Enhancing Hydrogen Adsorption Capacity of Metal Organic Frameworks M(BDC)TED$_{0.5}$ through Constructing a Bimetallic Structure

Renjie Li,[#] Xin Han,[#] Qiaona Liu, An Qian, Feifei Zhu, Jiawen Hu, Jun Fan, Haitao Shen,* Jichang Liu,* Xin Pu, Haitao Xu, and Bin Mu

ACCESS | 📊 Metrics & More | 📖 Article Recommendations | 🆂🅸 Supporting Information

ABSTRACT: Metal organic frameworks (MOFs) have promising application prospects in the field of hydrogen storage. However, the successful application of MOFs in the field is still limited by their hydrogen storage capacity. Herein, a series of M$_x$M$_{1-x}$(BDC)TED$_{0.5}$ (M = Zn, Cu, Co, or Ni) with a bimetallic structure was constructed by introducing two metal ions in the synthesis process. The results of X-ray diffraction, scanning electron microscopy, energy-dispersive spectroscopy, X-ray photoelectron spectroscopy, and inductively coupled plasma showed that the bimetallic structure with different content ratios can be stably constructed by a hydrothermal method. Among them, the Cu-based bimetal MOFs Cu$_{0.625}$Ni$_{0.375}$(BDC)TED$_{0.5}$ exhibited the best hydrogen storage capacity of 2.04 wt% at 77 K and 1 bar, which was 22% higher than that of monometallic Ni(BDC)TED$_{0.5}$. The enhanced hydrogen storage capacity can be attributed to the improved specific surface area and micropore volume of bimetal MOFs by introducing an appropriate amount of bimetallic atoms.

1. INTRODUCTION

With the increasingly severe environmental problems and the gradual exhaustion of fossil energy, the development of renewable clean energy to replace nonrenewable traditional fossil energy is becoming an inevitable trend. Among the many clean energy sources, hydrogen energy has become a research hotspot in recent years because of its advantages such as high calorific value, abundant reserves, and pollution-free nature.[1] However, the development of the hydrogen energy industry is limited by the hydrogen storage technology, which is one of the bottlenecks restricting the development of hydrogen energy due to its shortcomings of flammability, explosiveness, and difficulty in liquefaction. Therefore, the development of an efficient hydrogen storage technology has become particularly important.

At present, the methods of hydrogen storage include high-pressure gaseous hydrogen storage, low-temperature liquid hydrogen storage, physical adsorption hydrogen storage,[2,3] chemical adsorption hydrogen storage,[4] and liquid organic compound hydrogen storage.[5,6] Among them, physical adsorption hydrogen storage has become an important development direction because of its advantages such as low cost, high reversibility, and stability.[7] Porous carbon materials,[8] metal organic frameworks (MOFs),[9,10] and covalent organic frameworks[11] are commonly used as carriers for hydrogen physical adsorption. Particularly, MOFs with a large specific surface area, high porosity, and easy adjustment of the pore structure showed better hydrogen physical adsorption capacity,[12] and there have been several research studies on hydrogen storage of MOFs in the past 20 years.[13,14]

However, the theoretical physical hydrogen adsorption capacity of MOFs is far from being realized, and more

research on their industrial application of hydrogen storage is needed. Among the many methods to improve the hydrogen storage capacity of MOFs, organic ligand modification or introducing other metal ions into MOFs for constructing bimetallic structures is an effective method to optimize the performance of materials. The hydrogen adsorption capacity of Ni-Cu-BTC (BTC: trimesic acid) and Zn-Cu-BTC reported by Abdul et al.[2] reached 1.60 and 1.63 wt% at 77 K and 1 bar, which was 60% higher than that of Cu-BTC (1.02 wt%). This improvement in hydrogen adsorption capacity is attributed to the increase in the interaction force between hydrogen and MOFs caused by the introduction of bimetallic structures. In addition, previous studies also found that the introduction of bimetallic structures may be beneficial to expand the pore structure of MOFs. For example, compared with Zn-ZIF-8, the specific surface area and pore volume of Co-Zn-ZIF-8 reported by Kaur et al. increased by 40 and 33%, which improved the hydrogen adsorption performance of the Zn-ZIF-8 from 1.26 to 1.55 wt%.[15]

In 2004, Dybtsev et al.[16] first synthesized Zn(BDC)TED$_{0.5}$ using the hydrothermal method by dissolving zinc nitrate, terephthalic acid, and triethylenediamine in *N,N*-dimethylformamide. Subsequently, the researchers synthesized a series of M(BDC)TED$_{0.5}$ materials with different metals using nickel

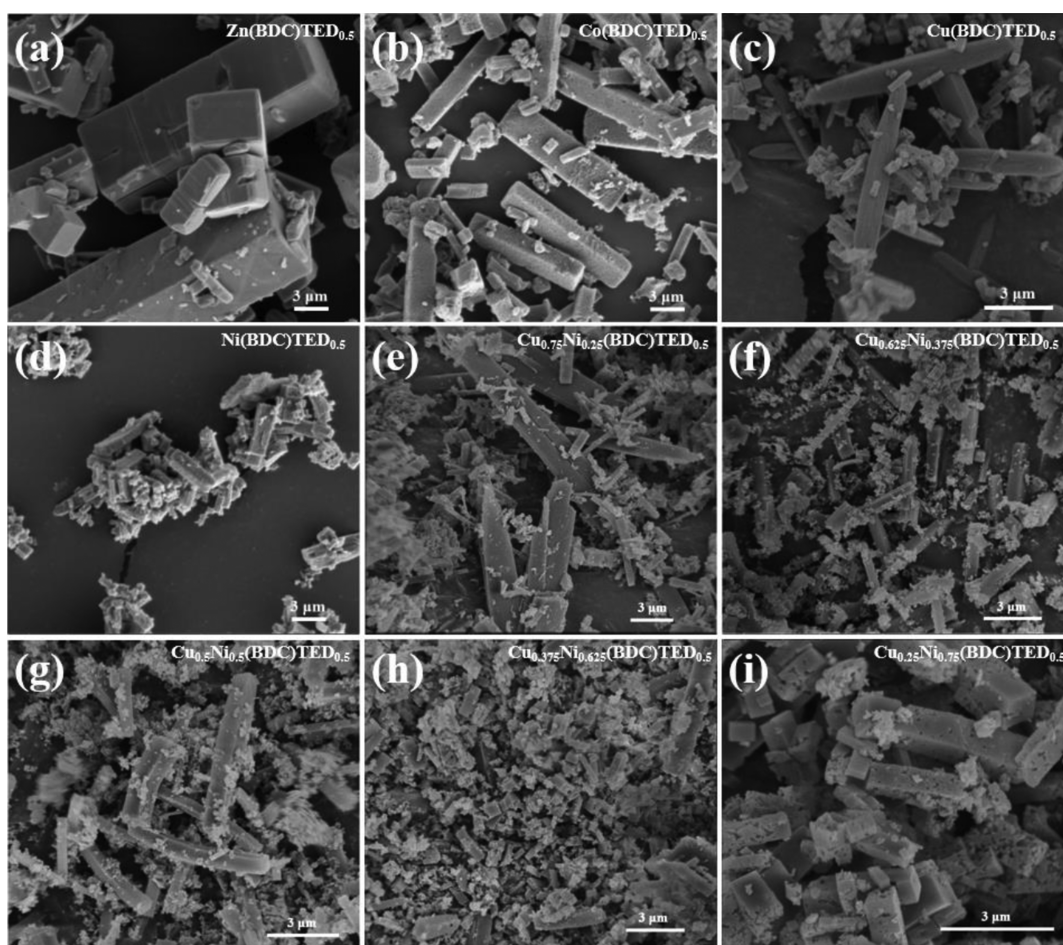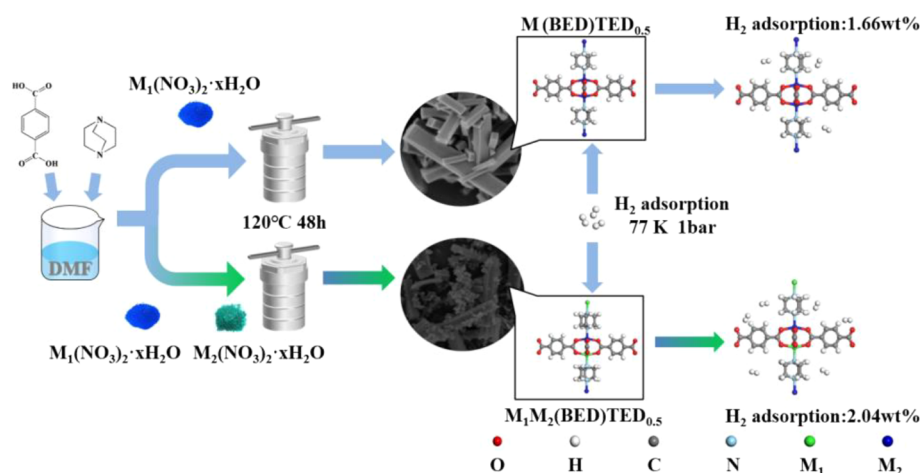**Scheme 1. Main Synthesis Process of M(*BDC*)TED$_{0.5}$ Samples**

Figure 1. SEM images of the synthesized M(*BDC*)TED$_{0.5}$ (a−d) and M$_x$M$_{1-x}$(*BDC*)TED$_{0.5}$ (e−i).

nitrate,[17] cobalt nitrate,[18] or copper nitrate[18] instead of zinc nitrate as a metal source. The results showed that M(*BDC*)-TED$_{0.5}$ (M = Cu, Zn, Co, Ni) is a flexible MOF with a stable structure and uniform pore size distribution and considered to have good application prospects in the field of hydrogen storage.

As mentioned above, the construction of bimetallic structures is an effective method to improve the gas adsorption capacity of MOFs, and previous studies had shown that bimetallic M(*BDC*)TED$_{0.5}$ could be successfully prepared. For

example, Poryvaev et al. tried to synthesize Cu$_{0.007}$Zn$_{1.993}$(*BDC*)TED$_{0.5}$ and studied the adsorption sites of several kinds of gases on the MOFs, elucidating that most of the gas resides in the centers of the cavities.[19] Therefore, it is a practical method to enhance the hydrogen storage capacity of M(*BDC*)TED$_{0.5}$. However, there is no report on the gas adsorption capacity of M(*BDC*)TED$_{0.5}$ modified with a series of different bimetallic structures.

Herein, a series of monometallic M(*BDC*)TED$_{0.5}$ was first prepared using a hydrothermal method, and then other metal

ions were introduced during the synthesis process to synthesize bimetallic $M_xM_{1-x}(BDC)TED_{0.5}$ (M = Zn, Cu, Co, or Ni) with a developed pore structure and hydrogen adsorption capacity. The results show that the hydrogen adsorption capacity and thermal stability of Cu-based bimetallic MOFs were significantly improved. The main innovation of this paper is to improve the pore structure of $M(BDC)TED_{0.5}$ series materials by constructing a bimetallic structure for the first time. The effects of metal species and bimetal atomic ratios on the crystal structure, micromorphology, pore structure, and hydrogen adsorption capacity of $M(BDC)TED_{0.5}$ have been thoroughly studied. The overall modification method is simple and convenient, providing new ideas for optimizing the properties of MOFs.

2. RESULTS AND DISCUSSION

2.1. Synthesis and Characterization of $M(BDC)TED_{0.5}$.
$M(BDC)TED_{0.5}$ and $M_xM_{1-x}(BDC)TED_{0.5}$ were synthesized by a hydrothermal method, as shown in Scheme 1. During the crystallization process of $M(BDC)TED_{0.5}$ samples, the metal cluster MO_4 was bridged with terephthalic acid to form a layered 2D structure, and triethylenediamine was used as a pillar in the longitudinal direction to expand the 2D plane into a 3D structure (Figure S1)[16] and thus produced a cavity that can be used for gas storage. As mentioned above, constructing bimetallic MOFs by introducing other metal ions into the structure may lead to a more developed pore structure and stronger adsorption sites. Because Zn, Cu, Co, and Ni can individually form $M(BDC)TED_{0.5}$ with a similar structure, it is possible to introduce another metal into $M(BDC)TED_{0.5}$ to cause isostructural substitution and form $M_xM_{1-x}(BDC)-TED_{0.5}$ with a bimetallic structure. The synthesis steps of bimetal MOFs (as shown in Scheme 1) are similar to those of monometallic MOFs and the difference is that two nitrates are used at the same time when synthesizing bimetal MOFs while only one is used when synthesizing monometallic MOFs. To systematically explore the effect of different metals on the hydrogen adsorption capacity of M $(BDC)TED_{0.5}$ and $M_xM_{1-x}(BDC)TED_{0.5}$, monometallic $M(BDC)TED_{0.5}$ (M = Zn, Cu, Co, or Ni) were first synthesized and tested for hydrogen adsorption capacity. Then, six kinds of bimetal $M_{0.5}M_{0.5}(BDC)TED_{0.5}$, such as $Cu_{0.5}Ni_{0.5}(BDC)TED_{0.5}$ and $Cu_{0.5}Zn_{0.5}(BDC)TED_{0.5}$, were synthesized to explore the change of the structure and hydrogen adsorption capacity for the MOFs. Finally, a series of $M_xM_{1-x}(BDC)TED_{0.5}$ (x = 0.250, 0.375, 0.500, 0.625, and 0.750) were synthesized by adjusting the ratio of different metals to study the effects of different metals and metal ratios on their physical hydrogen adsorption capacity.

The samples were first characterized by scanning electron microscopy (SEM) and X-ray diffraction (XRD) to study the structure and morphology, and the results are shown in Figures 1 and 2. Figure 1a−d demonstrate the surface morphologies of four monometallic $M(BDC)TED_{0.5}$ (M = Zn, Cu, Co, or Ni). $Zn(BDC)TED_{0.5}$ and $Co(BDC)TED_{0.5}$ have a rectangular parallelepiped morphology with regular crystal shape and smooth surface, and the crystal size ranges from 3 to 20 μm, which is similar to the morphology previously reported by Peng et al.[20] Although $Ni(BDC)TED_{0.5}$ is also mainly rectangular parallelepiped, its particle size with 3 μm is much smaller than that of the Zn and Co metal-based MOFs. Differently, the morphology of $Cu(BDC)TED_{0.5}$ was rod-shaped with small messy crystals attached to the surface, which
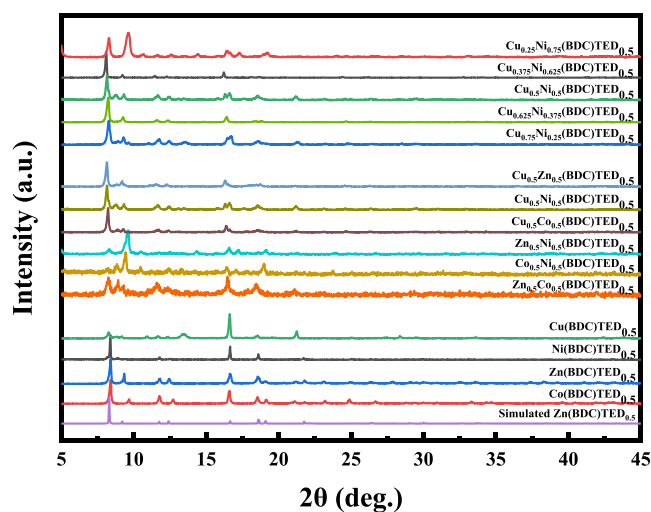

Figure 2. XRD pattern of $M(BDC)TED_{0.5}$ and $M_xM_{1-x}(BDC)TED_{0.5}$ samples.

is very different from the MOFs composed of other metals. In terms of the Cu-based bimetal MOFs, we can find that more small-particle crystals appear in bimetallic MOFs due to the competitive coordination of the two metals, and the morphology of the material is not as regular as that of several single-metal MOFs. $Cu_{0.625}Ni_{0.375}(BDC)TED_{0.5}$ and $Cu_{0.5}Ni_{0.5}(BDC)TED_{0.5}$ have the relatively regular slender cuboid morphology, with particle sizes ranging from 3 to 10 μm. The crystal morphology of $Cu_{0.25}Ni_{0.75}(BDC)TED_{0.5}$ and $Cu_{0.75}Ni_{0.25}(BDC)TED_{0.5}$ is more similar to that of $Ni(BDC)-TED_{0.5}$ and $Cu(BDC)TED_{0.5}$, which are needle-like and rectangular parallelepiped shapes, respectively. For the $Cu_{0.375}Ni_{0.625}(BDC)TED_{0.5}$ sample, the synthesized material under this ratio is also rectangular and has the smallest particle size. Some of the larger particles have a particle size of about 3 μm, and the remaining small particles are less than 1 μm, and the agglomeration phenomenon is more obvious. Furthermore, according to the analysis results of energy-dispersive spectroscopy (EDS) mapping in Figure S2, both metals in all bimetal MOFs are evenly distributed in the entire MOF structure, confirming that the bimetal structure is successfully synthesized.

The diffraction peak positions of the synthesized $M(BDC)-TED_{0.5}$ are in good agreement with the simulated $Zn(BDC)-TED_{0.5}$ and the five diffraction peaks located at around 2θ = 8.2°, 9.2°, 11.7°, 12.4°, and 16.5° correspond to the (100), (001), (110), (101), and (200) planes.[21] XRD analysis results show that the crystal structures of $M(BDC)TED_{0.5}$ synthesized with different metal ions are similar, confirming the successful synthesis of $M(BDC)(TED)_{0.5}$. At the same time, there are also some differences in the crystal structure of $M(BDC)-TED_{0.5}$ with different metals. The diffraction peak of $Ni(BDC)TED_{0.5}$ at 9.2° almost disappeared, and the diffraction peak of $Co(BDC)TED_{0.5}$ at 9.2° appeared red-shifted. This may be attributed to the effect of different metal atomic radius, and the crystal structures of MOF materials undergo subtle changes. The XRD patterns of Cu(BDC) $TED_{0.5}$ are quite different, which is reflected in the significant decrease of the diffraction peak intensity at 8.2° and an increase at 16.5°, indicating that the main exposed crystal plane of the $Cu(BDC)TED_{0.5}$ crystal is transformed to (200). The crystal structure of bimetallic MOFs is jointly affected by the metal

Table 1. ICP Results of the $M_{0.5}M_{0.5}(BDC)TED_{0.5}$ Samples

sample	metal 1 (wt%)	metal 2 (wt%)	the ratio of M1/M2 (mol/mol)
$Cu_{0.5}Ni_{0.5}(BDC)TED_{0.5}$	13.0	9.3	1.28
$Cu_{0.5}Co_{0.5}(BDC)TED_{0.5}$	14.0	9.7	1.33
$Cu_{0.5}Zn_{0.5}(BDC)TED_{0.5}$	15.0	12.0	1.28
$Zn_{0.5}Co_{0.5}(BDC)TED_{0.5}$	13.0	10.0	1.17
$Zn_{0.5}Ni_{0.5}(BDC)TED_{0.5}$	13.0	11.0	1.06
$Co_{0.5}Ni_{0.5}(BDC)TED_{0.5}$	11.0	12.0	0.91
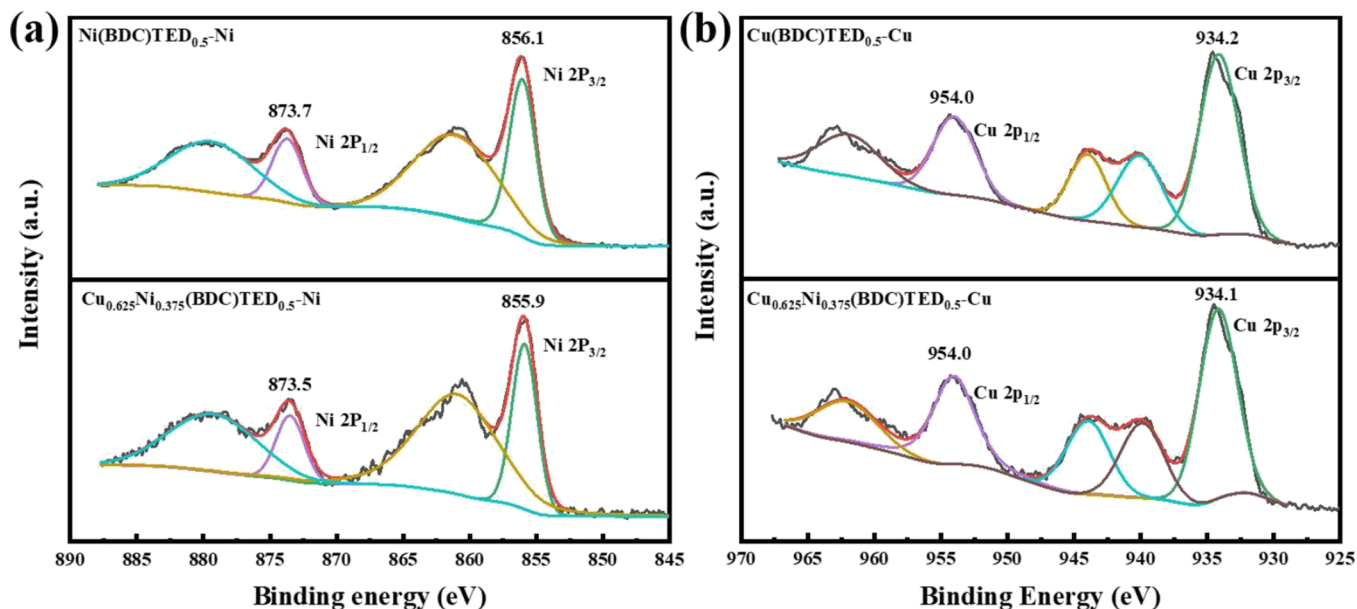
Figure 3. High-resolution (a) Ni 2p and (b) Cu 2p X-ray photoelectron spectroscopy (XPS) spectrum of Cu- or Ni-based $M(BDC)TED_{0.5}$ samples.

species and the bimetallic atomic ratio. The position and relative intensity of diffraction peaks of the three copper-contaning $M_{0.5}M_{0.5}(BDC)TED_{0.5}$ and $Cu_xNi_{1-x}(BDC)TED_{0.5}$ series materials (except for $Cu_{0.25}Ni_{0.75}(BDC)TED_{0.5}$) have no obvious change, indicating that the introduction of an appropriate amount of copper ions into $M(BDC)TED_{0.5}$ will not change the crystal structure. The diffraction peak position of $Zn_{0.5}Co_{0.5}(BDC)TED_{0.5}$ is still the same as that of $M(BDC)TED_{0.5}$, but the diffraction peak appears to be broadened, which may be attributed to the reduction of the crystal size. The diffraction peaks at 9.2° of $Co_{0.5}Ni_{0.5}(BDC)TED_{0.5}$ appeared red-shifted, and the competitive coordination of the two metal ions may cause lattice distortion, and the main exposed crystal plane of the crystal is also transformed to (001). The same phenomenon also appears in $Zn_{0.5}Ni_{0.5}(BDC)TED_{0.5}$ and $Cu_{0.25}Ni_{0.75}(BDC)TED_{0.5}$. Fourier transform infrared (FT-IR) characterization was also performed on $M(BDC)TED_{0.5}$, and the result is shown in Figure S3. FT-IR analysis displayed that using different metal ions to synthesize $M(BDC)TED_{0.5}$ has no significant impact on the structure.

Inductively coupled plasma (ICP) analysis was performed on the $M_{0.5}M_{0.5}(BDC)TED_{0.5}$ samples to investigate the element content in the bimetal MOFs; the results are shown in Table 1. We can see that the metal atom ratio in the actual material is different from 1:1 used in synthesis, which indicates that different metal ions have different interaction forces with organic ligands. Among these metal ions, Cu^{2+} ions have the strongest electron-withdrawing ability, and it is easier to form

stable complexes,[22] resulting in a higher proportion of copper ions in $M_{0.5}M_{0.5}(BDC)TED_{0.5}$.

XPS characterization was performed on $Ni(BDC)TED_{0.5}$, $Cu(BDC)TED_{0.5}$, and $Cu_{0.625}Ni_{0.375}(BDC)TED_{0.5}$ as typical samples to study the states of Ni and Cu elements in the $M(BDC)TED_{0.5}$, and the XPS spectra of Ni 2p and Cu 2p are shown in Figure 3. Figure 3a shows that the Ni element in $Ni(BDC)TED_{0.5}$ has two spin-orbit doublets at 856.1 and 873.7 eV, and the Ni element in $Cu_{0.625}Ni_{0.375}(BDC)TED_{0.5}$ has two spin-orbit doublets at 855.9 and 873.5 eV. The binding energy above is assigned to Ni $2p_{3/2}$ and Ni $2p_{1/2}$ peaks of Ni^{2+}, respectively, and the characteristic peaks around 861.0 and 879.6 eV belong to the satellite peaks of Ni^{2+}.[23] Figure 3b shows that in monometallic and bimetallic MOFs, the binding energies of the Cu element are almost the same, which has obvious characteristic peaks at 934.1−934.2 eV and 954.0 eV, corresponding to the Cu $2p_{3/2}$ and Cu $2p_{1/2}$ peaks of Cu^{2+}, and other peaks in the range of 935−965 eV belong to the satellite peaks of Cu^{2+}.[24] The results show that metal ions exist in divalent form in both monometallic MOFs and bimetallic MOFs, and the introduction of bimetals does not change the chemical state of metal ions.

Thermal analysis was performed on four kinds of $M(BDC)TED_{0.5}$ and three kinds of Cu-based bimetal $M_{0.5}M_{0.5}(BDC)TED_{0.5}$ with better hydrogen adsorption capacity to investigate their thermal stability, and the results are shown in Figure S4. The thermogravimetric (TG) curve showed a two-step weight loss in the range of 25−600 °C. Below 200 °C, the weight loss is mainly due to the removal of adsorbed water and *N,N*-
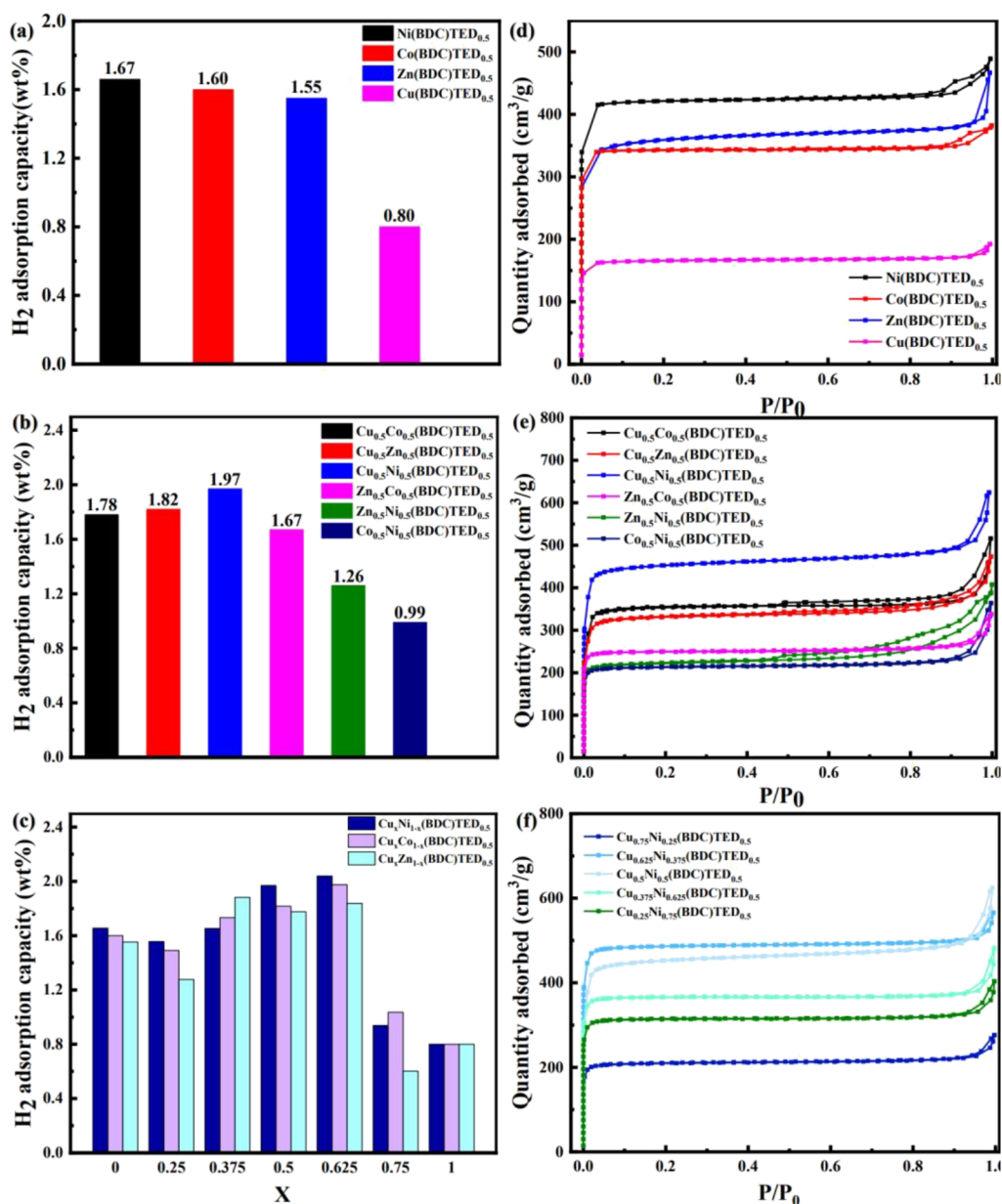
Figure 4. Hydrogen adsorption capacity of (a) M(*BDC*)TED$_{0.5}$, (b) M$_{0.5}$M$_{0.5}$(BDC)TED$_{0.5}$, and (c) different metal ratio M$_x$M$_{1-x}$(*BDC*)TED$_{0.5}$; nitrogen adsorption−desorption isotherms of (d) M(*BDC*)TED$_{0.5}$, (e) M$_{0.5}$M$_{0.5}$(BDC)TED$_{0.5}$, and (f) Cu$_x$Ni$_{1-x}$(*BDC*)TED$_{0.5}$.

dimethylformamide (DMF) molecules. When the temperature exceeds 250 °C, the frame of the material gradually begins to collapse, and the rate of weight loss increases significantly. Among the monometallic MOFs, Cu(*BDC*)TED$_{0.5}$ has the worst thermal stability and begins to decompose at 300 °C while Ni(*BDC*)TED$_{0.5}$ has the best thermal stability, which can reach up 400 °C. Because of the introduction of Ni ions with good thermal stability, the thermal stability of Cu$_{0.5}$Ni$_{0.5}$(BDC)TED$_{0.5}$ has improved compared to that of Cu(*BDC*)TED$_{0.5}$, and the structure can remain stable at 350 °C. All in all, although the introduction of bimetals may lead to a decrease in the thermal stability of MOFs, the MOFs still maintain a high stability and satisfy the usage conditions for hydrogen storage.

According to the above results, monometallic M(*BDC*)-TED$_{0.5}$ and bimetallic M$_x$M$_{1-x}$(*BDC*)TED$_{0.5}$ have been successfully synthesized by a simple hydrothermal method.

The monometallic MOFs are more regular in morphology and have a larger particle size while the bimetallic MOFs have a smaller particle size and a more disorderly crystal morphology with two metals evenly distributed in the structure. The introduction of bimetals did not change the crystal structure of the MOFs and the chemical properties of the metal and still maintained good thermal stability. These are all favorable for their use as a hydrogen storage material.

2.2. Gas Adsorption Capacity of M(*BDC*)TED$_{0.5}$. The hydrogen adsorption capacity and nitrogen adsorption−desorption isotherms were tested under the conditions of 77 K and 0−1 bar. The adsorption experiment results are summarized in Figure 4, and the hydrogen adsorption isotherms are shown in Figures S5 and S6. The Langmuir model assumes that the gas is adsorbed on the surface of the material as a monolayer. However, on the surface of many porous materials, adsorption was observed to occur in

Table 2. Specific Surface Area and Pore Parameters of M(BDC)TED$_{0.5}$

sample	S_{BET} (m^2/g)	$S_{Langmuir}$ (m^2/g)	pore volume (cm^3/g)	micropore volume (cm^3/g)	average pore size (nm)
Zn(BDC)TED$_{0.5}$	1089	1657	0.593	0.531	2.17
Ni(BDC)TED$_{0.5}$	1259	1874	0.696	0.645	2.21
Co(BDC)TED$_{0.5}$	1019	1507	0.552	0.528	2.17
Cu(BDC)TED$_{0.5}$	496	738	0.267	0.253	2.16

Table 3. Specific Surface Area and Pore Parameters of M$_{0.5}$M$_{0.5}$(BDC)TED$_{0.5}$

sample	S_{BET} (m^2/g)	$S_{Langmuir}$ (m^2/g)	pore volume (cm^3/g)	micropore volume (cm^3/g)	average pore size (nm)
Cu$_{0.5}$Ni$_{0.5}$(BDC)TED$_{0.5}$	1740	1993	0.966	0.656	2.22
Cu$_{0.5}$Co$_{0.5}$(BDC)TED$_{0.5}$	1380	1566	0.798	0.539	2.31
Cu$_{0.5}$Zn$_{0.5}$(BDC)TED$_{0.5}$	1326	1460	0.732	0.486	2.20
Zn$_{0.5}$Co$_{0.5}$(BDC)TED$_{0.5}$	1020	1088	0.523	0.380	2.05
Zn$_{0.5}$Ni$_{0.5}$(BDC)TED$_{0.5}$	892	979	0.630	0.314	2.82
Co$_{0.5}$Ni$_{0.5}$(BDC)TED$_{0.5}$	865	933	0.563	0.319	2.60

Table 4. Specific Surface Area and Pore Parameters of Cu$_x$Ni$_{1-x}$(BDC)TED$_{0.5}$

sample	S_{BET} (m^2/g)	$S_{Langmuir}$ (m^2/g)	pore volume (cm^3/g)	micropore volume (cm^3/g)	average pore size (nm)
Cu$_{0.75}$Ni$_{0.25}$(BDC)TED$_{0.5}$	850	918	0.427	0.313	2.00
Cu$_{0.625}$Ni$_{0.375}$(BDC)TED$_{0.5}$	1952	2128	0.875	0.738	1.79
Cu$_{0.5}$Ni$_{0.5}$(BDC)TED$_{0.5}$	1740	1993	0.966	0.656	2.22
Cu$_{0.375}$Ni$_{0.625}$(BDC)TED$_{0.5}$	1473	1598	0.745	0.565	2.02
Cu$_{0.25}$Ni$_{0.75}$(BDC)TED$_{0.5}$	1284	1369	0.624	0.480	2.22

multilayers instead of a monolayer. Brunauer, Emmett, and Teller proposed a multilayer adsorption model (BET) based on the basic Langmuir model. Both the Langmuir model and the BET model are commonly used methods to characterize the specific surface area of porous materials. Although the BET and Langmuir models do not accurately consider the interactions between adsorbate molecules, nor between the adsorbate molecules and the adsorbent molecules, the two models are commonly used to characterize the specific surface area of porous materials because of their simplicity.[25] The BET and Langmuir specific surface area and pore volume are summarized in Tables 234. According to the nitrogen adsorption isotherms in Figure 4, all the samples belong to the type-I adsorption isotherm, which are typical microporous materials and the adsorption capacity is determined by the pore volume. This indicates that the introduction of bimetals did not lead to changes in the pore structure of the samples.

Figure 4a shows the hydrogen adsorption capacity of the monometallic M(BDC)TED$_{0.5}$ samples, except for Cu(BDC)-TED$_{0.5}$ with a low adsorption capacity of 0.80 wt%; the hydrogen adsorption capacity of M(BDC)TED$_{0.5}$ has reached about 1.60 wt%. The Ni(BDC)TED$_{0.5}$ sample reaches the highest hydrogen adsorption capacity of 1.66 wt%. This huge difference in the capacity of hydrogen adsorption is also reflected in the specific surface area and pore volume. Among monometallic MOFs, Ni(BDC)TED$_{0.5}$ has the highest specific surface area of 1259 m^2/g and the largest micropore volume of 0.645 cm^3/g, while the specific surface area of Cu(BDC)-TED$_{0.5}$ is only 496 m^2/g and the pore volume of micropores is also the smallest. The fact that Ni(BDC)TED$_{0.5}$ shows a higher specific surface area and pore volume is consistent with previous experimental results.[20] The possible reason for the larger specific surface area of Ni(BDC)TED$_{0.5}$ is that the larger geometric pore volume or flexibility of the framework affects the adsorption capacity for small-molecule gases, thereby enhancing the material's nitrogen adsorption capacity.[21] On the opposite, Cu(BDC)TED$_{0.5}$ may have more framework

collapse or blockage under these synthesis conditions, which greatly reduces the gas adsorption capacity.

Previous studies have proved that the hydrogen adsorption capacity of MOFs is closely related to the specific surface area and micropore pore volume, larger specific surface area, and more micropore pore volumes which bring higher hydrogen adsorption capacity.[26,27] To further improve the pore structure, herein, M(BDC)TED$_{0.5}$ is modified by the method of constructing a bimetal structure. According to Figure 4b, the hydrogen adsorption capacity of several Cu-containing bimetallic MOFs has increased compared with that of the monometallic M(BDC)TED$_{0.5}$. Among them, Cu$_{0.5}$Ni$_{0.5}$(BDC)TED$_{0.5}$ has the most significant increase in hydrogen adsorption capacity, reaching 1.97 wt%, which is an increase of 146% compared with Cu(BDC)TED$_{0.5}$, and an increase of 18% compared with Ni(BDC)TED$_{0.5}$. In terms of pore structure, the Cu-containing bimetallic MOF samples also have an improvement in the specific surface area and micropore volume. The specific surface area of Cu$_{0.5}$Ni$_{0.5}$(BDC)TED$_{0.5}$ reaches 1740 m^2/g, which is 38% higher than that of Ni(BDC)TED$_{0.5}$. Under the combined effect of the increased specific surface area and micropore volume, the hydrogen adsorption capacity of the bimetallic MOFs is greatly increased. However, not all bimetal MOFs have improved hydrogen adsorption capacity, the hydrogen adsorption capacity of the bimetal MOFs synthesized by Zn−Co, Zn−Ni, and Co−Ni structure has no improvement. This may be attributed to the collapse or blockage of the framework during the synthesis process, resulting in a decrease in the specific surface area and pore volume, thereby reducing the hydrogen adsorption capacity.

The Cu-based bimetal MOFs with better hydrogen adsorption capacity were selected to study the optimal bimetal atomic ratio for their hydrogen adsorption capacity, and the results are shown in Figure 4c. Among the CuNi series samples, Cu$_{0.625}$Ni$_{0.375}$(BDC)TED$_{0.5}$ shows the highest hydrogen adsorption capacity, reaching 2.04 wt%, which is 22%

higher than that of Ni(BDC)TED$_{0.5}$. The improved hydrogen adsorption capacity also corresponds to its developed pore structure. Cu$_{0.625}$Ni$_{0.375}$(BDC)TED$_{0.5}$ has a huge specific surface area of 1952 m^2/g, and the micropore volume reaches 0.738 cm^3/g. The previously reported surface area of the M(BDC)TED$_{0.5}$ materials ranges from 1100 to 1800 m^2/g.[17,18] In this work, the improvement of the specific surface area of Cu$_{0.625}$Ni$_{0.375}$(BDC)TED$_{0.5}$ may be attributed to the two metal ions with different radii which make the pore structure of the material more diverse. Meanwhile, the Cu$_{0.625}$Co$_{0.375}$(BDC)-TED$_{0.5}$ and Cu$_{0.375}$Zn$_{0.625}$(BDC)TED$_{0.5}$ have also achieved the best hydrogen adsorption capacity in their bimetallic systems, reaching 1.98 and 1.88 wt%, respectively.

The hydrogen storage seams to occur via physisorption that obviously is a surface-related process. The hydrogen adsorption capacity provided by the unit BET specific surface area (H$_2$/S$_{BET}$) of each sample was analyzed and is shown in Figure 5. The H$_2$/S$_{BET}$ of M(BDC)TED$_{0.5}$ has no obvious
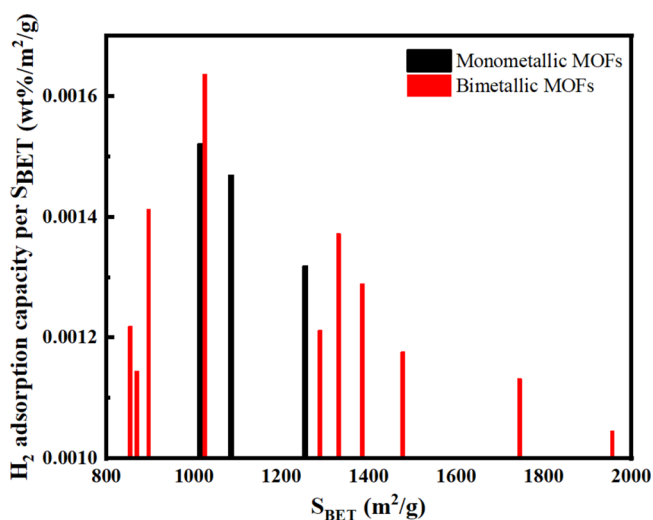

Figure 5. Hydrogen adsorption capacity provided by S$_{BET}$.

association with the monometallic or bimetallic structure, ranging from 0.0010 to 0.0016 wt%. M(BDC)TED$_{0.5}$ with S$_{BET}$ between 900 and 1400 m^2/g has a larger H$_2$/S$_{BET}$. The H$_2$/S$_{BET}$ of Zn$_{0.5}$Co$_{0.5}$(BDC)TED$_{0.5}$ reached 0.00164 wt%, which was the highest value among all samples. When S$_{BET}$ exceeds 1400 m^2/g, H$_2$/S$_{BET}$ gradually decreases with the increase of S$_{BET}$. Cu$_{0.625}$Ni$_{0.375}$(BDC)TED$_{0.5}$, which has the highest hydrogen adsorption capacity and the largest S$_{BET}$, has the smallest H$_2$/S$_{BET}$. Because H$_2$ is preferentially adsorbed on the sites with higher hydrogen affinity, the huge specific surface area of Cu$_{0.625}$Ni$_{0.375}$(BDC)TED$_{0.5}$ is difficult to be fully utilized for hydrogen adsorption.[31] However, as the adsorption pressure increases, the hydrogen adsorption capacity of MOFs is almost linearly related to the S$_{BET}$, so Cu$_{0.625}$Ni$_{0.375}$(BDC)-TED$_{0.5}$ has the greatest hydrogen storage potential.[15]

More detailed adsorption isotherm studies and adsorption thermodynamic calculations were carried out on the materials to further study the hydrogen adsorption behavior of MOF materials. The Langmuir, Freundlich, and Toth adsorption isotherm models were used to fit the hydrogen isotherms of Cu$_{0.625}$Ni$_{0.375}$(BDC)TED$_{0.5}$ at 77 and 273 K (Figure S7), respectively. The fitting parameters and correlation coefficient values are shown in Table 5.

Table 5. Model Parameters of Adsorption Isotherms of Hydrogen in Cu$_{0.625}$Ni$_{0.375}$(BDC)TED$_{0.5}$

	temperature	K	q$_m$	N	R^2
Langmuir	77	0.873	4.385		0.999
	273	0.056	0.161		0.999
Freundlich	77	2.078		1.438	0.996
	273	0.008		1.115	0.999
Toth	77	5.225	0.792	1.150	0.999
	273	0.001	2.417	0.196	0.999

The R^2 of the adsorption behavior of hydrogen molecules on Cu$_{0.625}$Ni$_{0.375}$(BDC)TED$_{0.5}$ fitted by Langmuir and Toth adsorption isotherms is above 0.999. Because the specific value of the parameter n in the Toth model needs to be determined by experimental data, which is inconvenient, the Langmuir model is finally used to fit the adsorption isotherm of hydrogen on MOFs. The hydrogen adsorption isotherm of Cu$_{0.625}$Ni$_{0.375}$(BDC)TED$_{0.5}$ can be approximated as the Langmuir model. This means that the adsorption of hydrogen takes place at specific homogeneous sites and hydrogen adsorbs on the MOF surface as a monolayer. According to the adsorption isotherm obtained by fitting the Langmuir model, the hydrogen adsorption heat (Q$_{st}$) on Cu$_{0.625}$Ni$_{0.375}$(BDC)TED$_{0.5}$ was calculated by the Clausius–Clapeyron equation and is shown in Figure 6. The Q$_{st}$ on Cu$_{0.625}$Ni$_{0.375}$(BDC)TED$_{0.5}$ is about 5.7−5.9 kJ/mol and nearly independent of hydrogen uptake, which is similar to the previous findings by Liu et al.[28]
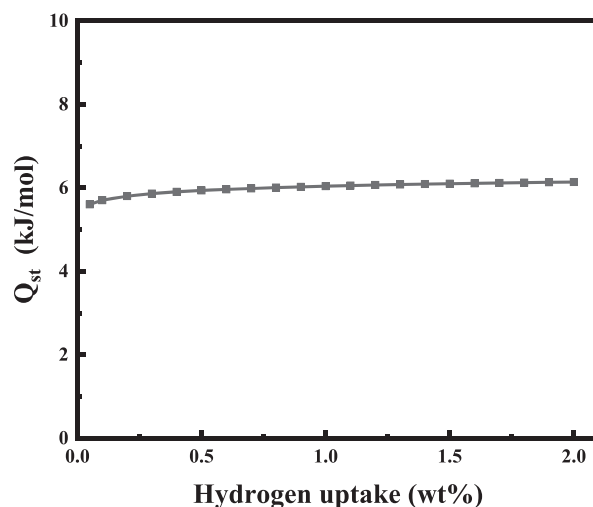

Figure 6. Hydrogen adsorption heat of Cu$_{0.625}$Ni$_{0.375}$ (BDC)TED$_{0.5}$ at 77 K.

The hydrogen adsorption capacity cycling test was performed on Cu$_{0.625}$Ni$_{0.375}$ (BDC)TED$_{0.5}$ as described in Section 4.5 to investigate the regeneration performance and adsorption stability of the adsorbent. Figure 7a shows four sets of hydrogen adsorption−desorption cycle isotherms of Cu$_{0.625}$Ni$_{0.375}$(BDC)TED$_{0.5}$. With the decrease of the adsorption pressure, the hydrogen adsorbed in Cu$_{0.625}$Ni$_{0.375}$(BDC)-TED$_{0.5}$ can be almost completely desorbed, indicating the good regeneration performance of the adsorbent. From Figure 7b, it can be seen that after 20 times adsorption−desorption processes, the hydrogen adsorption capacity of Cu$_{0.625}$Ni$_{0.375}$(BDC)TED$_{0.5}$ had no significant decrease and
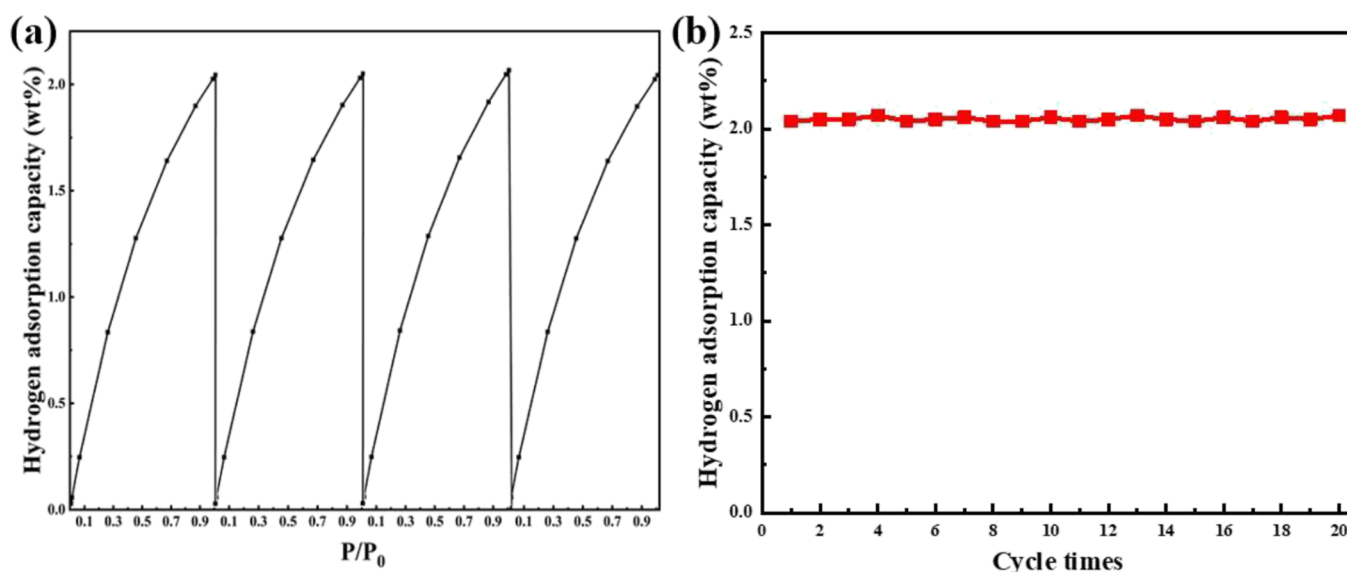
Figure 7. (a) Hydrogen adsorption−desorption isotherms. (b) Cyclic adsorption capacity of $Cu_{0.625}Ni_{0.375}(BDC)TED_{0.5}$.

Table 6. Hydrogen Adsorption Capacity Comparison of Selected MOFs at 77 K and 1 bar

MOFs	S_{BET} (m²/g)	micropore pore volume (cm³/g)	hydrogen adsorption capacity (wt%)	references
MOF-74(Mg)	1705		2.20	29
MOF-5	981	0.38	1.90	30
MOF-74(Zn)	850	0.39	2.16 (10 bar)	31
MIL-101(Cr)	1716	0.23	1.90	32
UIO-66	1186	0.49	1.50	32
Cu-BTC	945	0.40	1.12	2
Zn-ZIF-8	1131		1.26	15
Ni(BDC)TED$_{0.5}$	1259	0.65	1.66	this work
Cu/Ni-BTC	938	0.31	1.60	2
Cu/Zn-BTC	828	0.38	1.63	2
Co/Zn-ZIF-8	1571		1.55	15
Co$_{14}$Zn$_{86}$-MOF-74	1110	0.34	3.08 (10 bar)	31
Co$_{61}$Zn$_{39}$-MOF-74	820	0.39	2.73 (10 bar)	31
Cu$_{0.625}$Ni$_{0.375}$(BDC)TED$_{0.5}$	1952	0.74	2.04	this work
Cu$_{0.5}$Co$_{0.5}$(BDC)TED$_{0.5}$	1380	0.49	1.78	this work
Cu$_{0.5}$Zn$_{0.5}$(BDC)TED$_{0.5}$	1326	0.38	1.82	this work

remained at about 2.04 wt%. At the same time, the crystal structure of $Cu_{0.625}Ni_{0.375}(BDC)TED_{0.5}$ was also characterized (Figure S8), and the results showed that there was no obvious change in the XRD patterns before and after adsorption, indicating that hydrogen adsorption will not affect the crystal structure. The above analysis shows that the bimetal $M_xM_{1-x}(BDC)TED_{0.5}$ has good hydrogen adsorption stability.

2.3. Comparison of Hydrogen Adsorption Capacity with Other MOFs. Table 6 lists the hydrogen adsorption capacity, BET specific surface area, and micropore volume of some MOFs used for hydrogen storage. As mentioned above, the hydrogen adsorption capacity of MOFs is jointly affected by their specific surface area, pore volume, pore size and unsaturated metal sites. The specific surface area and pore structure of Cu-BTC and Cu-Zn-BTC are almost the same. With the introduction of Zn ions, the unsaturated metal sites in Cu-Zn-BTC increased, which increased the affinity between MOFs and hydrogen, thus increasing the hydrogen adsorption capacity from 1.12 to 1.63 wt%. The same phenomenon also appears in Zn-MOF-74, after the introduction of cobalt ions, the hydrogen adsorption capacity of the Co-Zn-MOF-74 is

greatly improved.[31] In addition, previous studies also found that the introduction of bimetallic structures may be beneficial to expand the pore structure of MOFs. The specific surface area of Zn-ZIF-8 increased from 1131 to 1571 m²/g after the introduction of cobalt ions, and the hydrogen adsorption capacity increased by 23%, reaching 1.55 wt%.[15] As shown in Table 5, Mg-MOF-74 not only possesses a large number of unsaturated metal sites but also has a developed pore structure, thus leading to a great hydrogen adsorption capacity of 2.2 wt %. Because of the relatively smaller interaction force between MOFs and hydrogen,[33] the hydrogen adsorption capacity of MOFs at 77 K and 1 bar is often lower than 2.5 wt%. The $Cu_{0.625}Ni_{0.375}(BDC)TED_{0.5}$ synthesized in this work has a hydrogen adsorption capacity of 2.04 wt% at 77 K and 1 bar. Compared with the bimetallic MOFs such as Co-Zn-ZIF-8 and Cu-Zn-BTC, the hydrogen adsorption capacity of $Cu_{0.625}Ni_{0.375}(BDC)TED_{0.5}$ is further improved and even close to the hydrogen adsorption capacity of CoZn-MOF-74 at 10 bar. Overall, $Cu_{0.625}Ni_{0.375}(BDC)TED_{0.5}$ accounts for a relatively higher hydrogen adsorption capacity in comparison with other MOFs under the same testing conditions. This improvement in

hydrogen adsorption capacity is attributed to the fully expanded pore structure due to the construction of the bimetallic structure, indicating that it is feasible to prepare porous materials with high hydrogen adsorption capacity by constructing bimetallic structure MOF materials.

In conclusion, the advantages of $Cu_{0.625}Ni_{0.375}(BDC)TED_{0.5}$ lie in high hydrogen adsorption capacity, good adsorption cycle, and improved thermal stability, and it is expected to be well applied in the field of hydrogen storage. However, previous studies have shown that the water stability of $M(BDC)TED_{0.5}$ series materials is generally poor, and long-term exposure to water molecules in the air will weaken the gas adsorption capacity of the materials.[34] Related issues remain to be further studied.

3. CONCLUSIONS

$M(BDC)TED_{0.5}$ (M = Zn, Cu, Co, Ni) were synthesized by the hydrothermal method and modified to improve the hydrogen adsorption capacity by constructing a bimetallic structure. The characterization results showed that introducing an appropriate amount of metal ions can isomorphically replace a part of metal ions in the samples of $Zn(BDC)TED_{0.5}$, $Co(BDC)TED_{0.5}$, and $Ni(BDC)TED_{0.5}$, which can still maintain the original crystal structure. The gas adsorption experiment proved that the introduction of a suitable bimetal structure into the $M(BDC)TED_{0.5}$ MOFs can not only effectively improve the physical hydrogen adsorption capacity but also has a significant impact on its physical properties such as specific surface area and pore size, which can explain the reason for the improvement of hydrogen adsorption capacity. Typically, among the bimetal MOFs, $Cu_{0.625}Ni_{0.375}(BDC)TED_{0.5}$ shows the largest specific surface area of 1952 m^2/g and the highest hydrogen adsorption capacity of 2.04 wt%, which is 22% higher than that of $Ni(BDC)TED_{0.5}$. The method of building a bimetallic structure to improve the hydrogen adsorption capacity of MOFs can provide new ideas for the optimization of the hydrogen adsorption capacity of MOFs.

4. EXPERIMENTAL SECTION

4.1. Experimental Chemicals. $Zn(NO_3)_2·6H_2O$ (98%), $Ni(NO_3)_2·6H_2O$ (99%), $Co(NO_3)_2·6H_2O$ (99%), and $Cu(NO_3)_2·6H_2O$ (99%) were purchased from Shanghai Titan Technology Co., Ltd. 1,4 phthalic acid (H_2BDC, 99%), 1,4-diazabicyclo[2.2.2] octane (TED, 98%), DMF (99%), and methanol (98%) were purchased from Beijing Yinuokai Technology Co., Ltd. All chemicals were used directly without further purification.

4.2. Synthesis of $M(BDC)TED_{0.5}$. The synthesis method of $M(BDC)TED_{0.5}$ adopted the previously reported experimental procedure,[34] and here $Zn(BDC)TED_{0.5}$ is taken as an example to introduce the synthesis method. First, a certain mass of zinc nitrate hexahydrate (1.44 g), terephthalic acid (H_2BDC, 0.54 g), and 1,4-diazabicyclo[2.2.2]octane (TED, 0.91 g) was dissolved in 50 mL of DMF. The incompletely dissolved mixed solution was transferred to ultrasonic treatment for 15 min, and then the mixed solution was placed in a magnetic stirrer and fully stir for 15 min until the solution clarifies. The solution was transferred to a 100 mL PTFE lining of the stainless steel reactor and kept at 120 °C for 48 h. After cooling the reactor to room temperature, the reaction solution was centrifuged at 11,000 rpm for 5 min, and the supernatant was washed with methanol three times. Then, the cleaned crystals

were vacuum-dried at 100 °C for 12 h to obtain the $Zn(BDC)TED_{0.5}$ sample. The other $M(BDC)TED_{0.5}$ was synthesized by replacing zinc nitrate hexahydrate with the same molar amount of corresponding nitrate hydrate.

4.3. Synthesis of Bimetal $M_xM_{1−x}(BDC)TED_{0.5}$. The synthesis method of $M_xM_{1−x}(BDC)TED_{0.5}$ is similar to that of $M(BDC)TED_{0.5}$. First, a certain amount of two metal nitrate hydrates (total 4.9 mmol), terephthalic acid (0.54 g), and 1,4-diazabicyclo[2.2.2]octane (0.91 g) were dissolved in 50 mL N,N-dimethylformamide. Then, the resultant mixture was subjected to ultrasonic treatment for 15 min and stirred for 15 min until the solution is clear. The subsequent crystallization and activation process is consistent with monometallic $M(BDC)TED_{0.5}$ and the detailed synthesis method is shown in the Supporting Information.

4.4. Characterization. Powder XRD patterns were obtained on a RigakuD/max 2550 VB/PC, and the 2θ range was from 5° to 80°. ICP mass spectrometry analysis was performed on an Inductively Coupled Plasma Atomic Emission Spectrometer. FT-IR analysis was performed on a Nicolet 6700 Fourier Infrared Spectrometer. SEM and EDS were performed on a GeminiSEM 500 field emission to scan electron microscope. The surfaces were characterized using a Thermo ESCALAB 250XI XPS system. TG analysis was carried out on the thermogravimetric-differential thermal simultaneous thermal analyzer STA 449 F3, the test was carried out in nitrogen, the heating rate was 10 °C min^{-1}, and the test temperature range was 25−650 °C.

4.5. Hydrogen Adsorption Measurements. The hydrogen adsorption capacity was performed on a Micromeritics ASAP2460. All adsorption data were obtained using ultrahigh purity gases (99.999%). The physical adsorption experiment was carried out at 77 K and 0−1 bar. Before analysis, the MOF samples (100 mg) were outgassed in the analysis tube under vacuum with heating up to 170 °C, which is sufficient to remove solvent molecules without thermal decomposition or loss of framework crystallinity.

During the hydrogen cycle adsorption test, the samples were continuously subjected to adsorption−desorption operations for 20 cycles, and the hydrogen adsorption capacity of the samples was recorded when the pressure was 1 bar each time.

4.6. Nitrogen Adsorption Measurements. The nitrogen adsorption isotherm, specific surface area, and pore structure data were recorded on a Micromeritics ASAP2460. All adsorption data were obtained using ultrahigh-purity gases (99.999%). The physical adsorption experiment was carried out at 77 K and 0−1 bar. The nitrogen adsorption data used calculation of the apparent surface areas based on BET equations, and the pore structure based on Barrett−Joyner−Halenda equations.

4.7. Adsorption Isotherm Model. Equilibrium relationships between the adsorbent and adsorbate are described by adsorption isotherms. The hydrogen adsorption isotherms of MOFs are fitted by Langmuir and Freundlich and Toth adsorption isotherms.[35]

The Langmuir isotherm is given as:

$$q_e = \frac{q_m KP}{1 + KP} \tag{1}$$

where q_e, q_m, K, and P are the hydrogen adsorption capacity, maximum adsorption capacity, Langmuir constant, and equilibrium pressure.

The Freundlich isotherm is given as:

$$q_e = KP^{1/n} \tag{2}$$

where q_e, K, P, and n are the hydrogen adsorption capacity, adsorption equilibrium constant, adsorption pressure, and adsorption intensity constant.

The Toth adsorption isotherm is given as:

$$q_e = \frac{q_m KP}{(1 + (KP)^n)^{1/n}} \tag{3}$$

where q_e, q_m, K, P, and n are the hydrogen adsorption capacity, maximum adsorption capacity, adsorption equilibrium constant, adsorption pressure, and surface property parameter.

According to the adsorption isotherm equation, the hydrogen adsorption heat on the MOFs is calculated by the Clausius−Clapeyron equation:

$$\frac{Q_{st}}{R} = \frac{d(\ln P_{H_2})}{d\left(\frac{1}{T}\right)} \tag{4}$$

where Q_{st}, R, T, and P_{H2} are the hydrogen adsorption heat, gas constant, hydrogen adsorption temperature, and hydrogen adsorption equilibrium pressure.

■ ASSOCIATED CONTENT

Ⓢⓘ Supporting Information
The Supporting Information is available free of charge at https://pubs.acs.org/doi/10.1021/acsomega.2c01914.

Schematic diagram of $Zn(BDC)TED_{0.5}$ unit cell structure, EDS analysis, IR analysis TG analysis, hydrogen adsorption isotherms, and XRD patterns (PDF)

■ AUTHOR INFORMATION

Corresponding Authors
Haitao Shen − State Key Laboratory of Chemical Engineering, School of Chemical Engineering, East China University of Science and Technology, Shanghai 200237, China; Email: htshen@ecust.edu.cn

Jichang Liu − State Key Laboratory of Chemical Engineering, School of Chemical Engineering, East China University of Science and Technology, Shanghai 200237, China; Key Laboratory for Green Processing of Chemical Engineering of Xinjiang Bingtuan, School of Chemistry and Chemical Engineering, Shihezi University, Shihezi 832003, China; orcid.org/0000-0002-5295-1778; Email: liujc@ecust.edu.cn

Authors
Renjie Li − State Key Laboratory of Chemical Engineering, School of Chemical Engineering, East China University of Science and Technology, Shanghai 200237, China; orcid.org/0000-0003-4280-5774

Xin Han − State Key Laboratory of Chemical Engineering, School of Chemical Engineering, East China University of Science and Technology, Shanghai 200237, China

Qiaona Liu − State Key Laboratory of Chemical Engineering, School of Chemical Engineering, East China University of Science and Technology, Shanghai 200237, China

An Qian − State Key Laboratory of Chemical Engineering, School of Chemical Engineering, East China University of Science and Technology, Shanghai 200237, China

Feifei Zhu − State Key Laboratory of Chemical Engineering, School of Chemical Engineering, East China University of Science and Technology, Shanghai 200237, China

Jiawen Hu − State Key Laboratory of Chemical Engineering, School of Chemical Engineering, East China University of Science and Technology, Shanghai 200237, China

Jun Fan − State Key Laboratory of Chemical Engineering, School of Chemical Engineering, East China University of Science and Technology, Shanghai 200237, China

Xin Pu − State Key Laboratory of Chemical Engineering, School of Chemical Engineering, East China University of Science and Technology, Shanghai 200237, China

Haitao Xu − State Key Laboratory of Chemical Engineering, School of Chemical Engineering, East China University of Science and Technology, Shanghai 200237, China; orcid.org/0000-0002-2785-2110

Bin Mu − School for Engineering of Matter, Transport, and Energy, Arizona State University, Tempe, Arizona 85287, United States; orcid.org/0000-0002-9117-1299

Complete contact information is available at:
https://pubs.acs.org/10.1021/acsomega.2c01914

Author Contributions
#R.L. and X.H. contribute equally to this paper and should be considered as co-first author.

Notes
The authors declare no competing financial interest.

■ ACKNOWLEDGMENTS

■ REFERENCES
(1) Han, X.; Si, T.; Liu, Q.; Zhu, F.; Li, R.; et al. 2D Bimetallic RuNi Alloy Co-Catalysts Remarkably Enhanced the Photocatalytic H_2 Evolution Performance of g-C_3N_4 Nanosheets. Chem. Eng. J. 2021, 426, No. 130824.

(2) Peedikakkal, A. M. P.; Aljundi, I. H. Mixed-Metal Cu-BTC Metal−Organic Frameworks as a Strong Adsorbent for Molecular Hydrogen at Low Temperatures. ACS Omega 2020, 5, 28493−28499.

(3) Tachikawa, H.; Izumi, Y.; Iyama, T.; Azumi, K. Molecular Design of a Reversible Hydrogen Storage Device Composed of the Graphene Nanoflake−Magnesium−H_2 System. ACS Omega 2021, 6, 7778−7785.

(4) Sato, T.; Mochizuki, T.; Ikeda, K.; Honda, T.; Otomo, T.; et al. Crystal Structural Investigations for Understanding the Hydrogen Storage Properties of $YMgNi_4$-Based Alloys. ACS Omega 2020, 5, 31192−31198.

(5) Sun, Q.; Wang, N.; Xu, Q.; Yu, J. Nanopore-Supported Metal Nanocatalysts for Efficient Hydrogen Generation from Liquid-Phase Chemical Hydrogen Storage Materials. Adv. Mater. 2020, 32, No. 2001818.

(6) Abdin, Z.; Tang, C.; Liu, Y.; Catchpole, K. Large-Scale Stationary Hydrogen Storage via Liquid Organic Hydrogen Carriers. iScience 2021, 24, No. 102966.

(7) Ramimoghadam, D.; Gray, E. M.; Webb, C. J. Review of Polymers of Intrinsic Microporosity for Hydrogen Storage Applications. Int. J. Hydrogen Energy 2016, 41, 16944−16965.

(8) Liu, Z.; Xue, Q.; Ling, C.; Yan, Z.; Zheng, J. Hydrogen Storage and Release by Bending Carbon Nanotubes. Comput. Mater. Sci. 2013, 68, 121−126.

(9) Ahmed, A.; Siegel, D. J. Predicting Hydrogen Storage in MOFs via Machine Learning. *Patterns* **2021**, *2*, No. 100291.

(10) Gangu, K. K.; Maddila, S.; Mukkamala, S. B.; Jonnalagadda, S. B. Characteristics of MOF, MWCNT and Graphene Containing Materials for Hydrogen Storage: A Review. *J. Energy Chem.* **2019**, *30*, 132−144.

(11) Kalidindi, S. B.; Fischer, R. A. Covalent Organic Frameworks and Their Metal Nanoparticle Composites: Prospects for Hydrogen Storage. *Phys. Status Solidi B* **2013**, *250*, 1119−1127.

(12) Giappa, R. M.; Tylianakis, E.; Di Gennaro, M.; Gkagkas, K.; Froudakis, G. E. A Combination of Multi-Scale Calculations with Machine Learning for Investigating Hydrogen Storage in Metal Organic Frameworks. *Int. J. Hydrogen Energy* **2021**, *46*, 27612−27621.

(13) Shet, S. P.; Priya, S. S.; Sudhakar, K.; Tahir, M. A Review on Current Trends in Potential Use of Metal-Organic Framework for Hydrogen Storage. *Int. J. Hydrogen Energy* **2021**, *46*, 11782−11803.

(14) Koizumi, K.; Nobusada, K.; Boero, M. Hydrogen Storage Mechanism and Diffusion in Metal-Organic Frameworks. *Phys. Chem. Chem. Phys.* **2019**, *21*, 7756−7764.

(15) Kaur, G.; Rai, R.; Tyagi, D.; Yao, X.; Li, P. Z.; Singh, S.; et al. Room-Temperature Synthesis of Bimetallic Co-Zn Based Zeolitic Imidazolate Frameworks in Water for Enhanced CO_2 and H_2 Uptakes. *J. Mater. Chem. A* **2016**, *39*, 14932−14938.

(16) Dybtsev, D.; Chun, H.; Kim, K. Rigid and Flexible: A Highly Porous Metal-Organic Framework with Unusual Guest-Dependent Dynamic Behavior. *Angew. Chem., Int. Ed.* **2004**, *43*, 5033−5036.

(17) Song, P.; Li, Y.; He, B.; Yang, J.; Zheng, J.; et al. Hydrogen Storage Properties of Two Pillared-Layer Ni(II) Metal-Organic Frameworks. *Microporous Mesoporous Mater.* **2011**, *142*, 208−213.

(18) Takei, T.; Kawashima, J.; Ii, T.; Maeda, A.; Hasegawa, M.; et al. Hydrogen Adsorption Properties of Lantern-Type Dinuclear M-(BDC)(DABCO)$_{1/2}$. *Bull. Chem. Soc. Jpn.* **2008**, *81*, 847−856.

(19) Poryvaev, A. S.; Sheveleva, A. M.; Demakov, P. A.; Arzumanov, S. S.; Stepanov, A. G.; et al. Pulse EPR Study of Gas Adsorption in Cu^{2+}-Doped Metal−Organic Framework [Zn$_2$(1,4-Bdc)$_2$(Dabco)]. *Appl. Magn. Reson.* **2018**, *49*, 255−264.

(20) Peng, L.; Wu, S.; Yang, X.; Hu, J.; Fu, X.; et al. Application of Metal Organic Frameworks M(Bdc)(Ted)$_{0.5}$ (M = Co, Zn, Ni, Cu) in the Oxidation of Benzyl Alcohol. *RSC Adv.* **2016**, *6*, 72433−72438.

(21) Xiang, H.; Ameen, A.; Gorgojo, P.; Siperstein, F. R.; Holmes, S. M.; et al. Selective Adsorption of Ethane over Ethylene on M(Bdc)(Ted)$_{0.5}$ (M = Co, Cu, Ni, Zn) Metal-Organic Frameworks (MOFs). *Microporous Mesoporous Mater.* **2020**, *292*, No. 109724.

(22) Li, K.; Xue, D. Estimation of Electronegativity Values of Elements in Different Valence States. *J. Phys. Chem. A* **2006**, *110*, 11332−11337.

(23) Yi, Y.; Zhang, P.; Qin, Z.; Yu, C.; Li, W.; et al. Low Temperature CO Oxidation Catalysed by Flower-like Ni−Co−O: How Physicochemical Properties Influence Catalytic Performance. *RSC Adv.* **2018**, *8*, 7110−7122.

(24) Hanke, M.; Arslan, H. K.; Bauer, S.; Zybaylo, O.; Christophis, C.; et al. The Biocompatibility of Metal−Organic Framework Coatings: An Investigation on the Stability of SURMOFs with Regard to Water and Selected Cell Culture Media. *Langmuir* **2012**, *28*, 6877−6884.

(25) Xiong, F.; Rother, G.; Gong, Y.; Moortgat, J. Reexamining Supercritical Gas Adsorption Theories in Nano-Porous Shales under Geological Conditions. *Fuel* **2021**, *287*, No. 119454.

(26) Kudiiarov, V.; Lyu, J.; Semenov, O.; Lider, A.; Chaemchuen, S.; et al. Prospects of Hybrid Materials Composed of MOFs and Hydride-Forming Metal Nanoparticles for Light-Duty Vehicle Hydrogen Storage. *Appl. Mater. Today* **2021**, *25*, No. 101208.

(27) Suh, M. P.; Park, H. J.; Prasad, T. K.; Lim, D. W. Hydrogen Storage in Metal-Organic Frameworks. *Chem. Rev.* **2012**, *112*, 782−835.

(28) Liu, J.; Lee, J. Y.; Pan, L.; Obermyer, R. T.; Simizu, S.; et al. Adsorption and Diffusion of Hydrogen in a New Metal−Organic Framework Material: [Zn(Bdc)(Ted)$_{0.5}$]. *J. Phys. Chem. C* **2008**, *112*, 2911−2917.

(29) Sumida, K.; Brown, C. M.; Herm, Z. R.; Chavan, S.; Bordiga, S.; et al. Hydrogen Storage Properties and Neutron Scattering Studies of Mg$_2$(Dobdc)—a Metal−Organic Framework with Open Mg^{2+} Adsorption Sites. *Chem. Commun.* **2011**, *47*, 1157−1159.

(30) Segakweng, T.; Musyoka, N. M.; Ren, J.; Crouse, P.; Langmi, H. W. Comparison of MOF-5- and Cr-MOF-Derived Carbons for Hydrogen Storage Application. *Res. Chem. Intermed.* **2016**, *42*, 4951−4961.

(31) Botas, J. A.; Calleja, G.; Sánchez-Sánchez, M.; Orcajo, M. G. Effect of Zn/Co Ratio in MOF-74 Type Materials Containing Exposed Metal Sites on Their Hydrogen Adsorption Behaviour and on Their Band Gap Energy. *Int. J. Hydrogen Energy* **2011**, *36*, 10834−10844.

(32) Ren, J.; Musyoka, N. M.; Langmi, H. W.; North, B. C.; Mathe, M.; et al. Fabrication of Core−Shell MIL-101(Cr)@UiO-66(Zr) Nanocrystals for Hydrogen Storage. *Int. J. Hydrogen Energy* **2014**, *39*, 14912−14917.

(33) Perles, J.; Iglesias, M.; Martín-Luengo, M.-Á.; Monge, M. Á.; Ruiz-Valero, C.; et al. Metal−Organic Scandium Framework: Useful Material for Hydrogen Storage and Catalysis. *Chem. Mater.* **2005**, *17*, 5837−5842.

(34) Pu, X.; Qin, X.; Han, Q.; Li, R.; Zhu, F.; et al. Preparation and Carbonization of Metal Organic Framework Zn(Bdc)(Ted)$_{(0.5)}$ for Enhancing Moisture Resistance and Methane Storage Capacity. *Ind. Eng. Chem. Res.* **2021**, *60*, 3809−3818.

(35) Foo, K. Y.; Hameed, B. H. Insights into the Modeling of Adsorption Isotherm Systems. *Chem. Eng. J.* **2010**, *156*, 2−10.